

# Automatic Detection and Visualization of Qualitative Hemodynamic Characteristics in Cerebral Aneurysms

Rocco Gasteiger, Dirk J. Lehmann, Roy van Pelt, Gábor Janiga,  
Oliver Beuing, Anna Vilanova, *Member, IEEE*, Holger Theisel, and Bernhard Preim

**Abstract**—Cerebral aneurysms are a pathological vessel dilatation that bear a high risk of rupture. For the understanding and evaluation of the risk of rupture, the analysis of hemodynamic information plays an important role. Besides quantitative hemodynamic information, also qualitative flow characteristics, e.g., the *inflow jet* and *impingement zone* are correlated with the risk of rupture. However, the assessment of these two characteristics is currently based on an interactive visual investigation of the flow field, obtained by computational fluid dynamics (CFD) or blood flow measurements. We present an automatic and robust detection as well as an expressive visualization of these characteristics. The detection can be used to support a comparison, e.g., of simulation results reflecting different treatment options. Our approach utilizes local streamline properties to formalize the inflow jet and impingement zone. We extract a characteristic seeding curve on the ostium, on which an inflow jet boundary contour is constructed. Based on this boundary contour we identify the impingement zone. Furthermore, we present several visualization techniques to depict both characteristics expressively. Thereby, we consider accuracy and robustness of the extracted characteristics, minimal visual clutter and occlusions. An evaluation with six domain experts confirms that our approach detects both hemodynamic characteristics reasonably.

**Index Terms**—Cerebral aneurysm, Hemodynamic, Inflow jet, Impingement zone, Visualization, Glyph.

## 1 INTRODUCTION

Cerebral aneurysms are pathological and local vessel dilatations which result from a congenital or evolved weakness of the vessel wall. They bear a high risk of rupture, with often fatal consequences for the patient. The aneurysm's geometric size is a measure for the risk of rupture: larger aneurysms are more likely to rupture than smaller aneurysms [37]. The majority of all ruptured aneurysms, however, are small (5-10 mm) and aneurysm morphology alone is not a reliable indicator to estimate the risk of rupture. The hemodynamics within the aneurysm play also an important role in aneurysm progression and rupture [33]. Thus, biomedical engineers and neuroradiologists who are involved in clinical research, are interested in the analysis of hemodynamic characteristics (obtained by CFD simulation or flow measurement). They focus on assessing the correlations between flow characteristics and the risk of rupture in order to optimize treatment options. The derived hemodynamic information are characterized by quantitative parameters, such as the wall shear stress (WSS), and qualitatively, e.g., with respect to the *inflow jet* and size of the *impingement zone*. The inflow jet consists of parallel inflow with high speed compared to other parts in the aneurysm. The impingement zone is the region on the aneurysm wall, where the inflow jet is seen to impact the wall for the first time with high speed.

In recent studies, it has been shown that the occurrence and the

shape of the inflow jet as well as the impingement zone are associated with the risk of rupture [5, 6]. A concentrated inflow jet with a small impingement zone increases the risk of a rupture. The assessment of qualitative characteristics is currently based on visual inspection only. Without automation, the reproducibility is low and a comparison, e.g., of different treatment options is difficult to conduct. With a reliable approach it would be possible to assess how a certain treatment influences the inflow jet and the impingement zone and to correlate these changes with the success of the treatment.

Thus, we focus in this paper on an automatic and robust detection and visualization of the inflow jet and its impingement zone. In particular, we derive a formal description of the inflow jet by utilizing local streamline properties and automatically extracting a characteristic inflow jet seeding curve. Based on this seeding curve, we integrate an inflow jet boundary contour and identify its impingement zone on the aneurysm wall. Summarizing, the main contributions of this paper are:

- An approach to automatically detect and extract a characteristic seeding curve, on which we construct an inflow jet boundary contour for steady flow datasets. Our approach utilizes local streamline properties to formalize the inflow jet and impingement zone detection. Based on the extracted inflow jet boundary contour, our approach localizes the impingement zone.
- Expressive visualization techniques for the inflow jet and the impingement zone along with the relevant anatomical context.
- An evaluation of our approach with six domain experts to qualitatively compare the automatically and manually extracted hemodynamic characteristics.

## 2 RELATED WORK

The visual exploration of blood flow data gains importance due to its essential role in pathological vessel development. Major application areas are the understanding of the cardiovascular system and their pathological variations. Biomedical researchers primarily employ established flow visualization techniques, like color-coded streamlines, probe planes, isosurfaces, and glyphs to get insight in the hemodynamic behavior [1, 5, 23]. For a survey of these basic flow visualization techniques, see Post et al. [29]. Subsequently, we discuss general flow visualization techniques applicable for the exploration of blood flow and we continue with developments dedicated to the exploration of cardiac and cerebral blood flow.

- Rocco Gasteiger and Bernhard Preim are with the department of Simulation and Graphics, within the group Visualization at the University of Magdeburg, Germany, E-mail: {rocco.gasteiger,bernhard.preim}@ovgu.de.
- Dirk J. Lehmann and Holger Theisel are with the department of Simulation and Graphics, within the group Visual Computing at the University of Magdeburg, Germany, E-mail: {dirk.lehmann,holger.theisel}@ovgu.de.
- Roy van Pelt and Anna Vilanova are with the department of Biomedical Engineering, within the group of Biomedical Image Analysis at Eindhoven University of Technology, E-mail: {r.f.p.v.pelt,a.vilanova}@tue.nl.
- Gábor Janiga is with the Institute of Fluid Dynamics and Thermodynamics at the University of Magdeburg, Germany, E-mail: janiga@ovgu.de.
- Oliver Beuing is with the department of Neuroradiology at the University Hospital Magdeburg, Germany, E-mail: oliver.beuing@med.ovgu.de.

Manuscript received 31 March 2012; accepted 1 August 2012; posted online 14 October 2012; mailed on 5 October 2012.

For information on obtaining reprints of this article, please send e-mail to: tvcg@computer.org.

**General Flow Visualization Techniques.** Flow visualization research has made rapid advances in the area of topology-based flow visualization methods. The survey articles from Laramée et al. [19, 20] discussed open issues in the practical application. In contrast to the detection of flow structure by using analytical definitions, Heideberg et al. [15] proposed an automatic pattern matching approach. They employ a set of idealized flow patterns, such as swirling flow or vortices, and compute a similarity of these patterns to the underlying vector field region, e.g., in aerodynamic applications. Other approaches are based on the identification of clusters, which represent potentially interesting flow regions [12, 18]. These clusters are extracted by characteristic scalar fields, like the bending energy of integral lines, or based on diffusion models. The resulting clusters can be represented in a multiscale visualization approach. For the description of flow behavior, Salzbrunn et al. [31] introduced line predicates, which are Boolean functions that return true if an integration line or a point of that line fulfills a specific feature. This concept provides a flexible method to identify a large variety of flow structures. Mattausch et al. [24] presented strategies for interactive exploration of 3D flow by adapting streamline seeding and visualization. They map flow attributes, such as speed and pressure, to line attributes, indicating interesting flow regions. Furthermore, they employ depth cues and focus-and-context methods, such as magic volumes, to enhance depth perception and to minimize occlusions.

Most of these techniques, however, are not adapted to specific medical diagnosis and research questions. This adaptation would include the extraction of anatomical landmarks to be used for streamline and pathline seeding as well as in-depth understanding of relevant flow properties to emphasize the related regions. Due to the complex geometry of vascular structures, complex flow patterns occur and it is challenging to avoid visual clutter.

**Exploration of Cardiac Blood Flow.** Due to the large diameter of the coronary vessels, in-vivo blood flow measurements are feasible [22]. The resulting unsteady flow data are noisy and exhibit various artifacts, e.g., phase wraps. With proper preprocessing [16] they have a great diagnostic potential. To exploit this potential, Van Pelt et al. [34, 35] employed illustrative rendering techniques, such as flow direction highlighting on interactive pathlines, and particles for visualization of measured blood flow data. They combine it with interaction schemes, such as semi-automatically placed seeding planes, and virtual probes to explore the flow. Born et al. [3] applied a user-defined line predicate to the analysis of measured cardiac blood flow data. For example, they enhance vortices and regions with fast flow to investigate pathological vessel morphology and its influence to the flow behavior. Our approach is inspired by line predicates as well.

**Exploration of Flow in Cerebral Aneurysms.** Neugebauer et al. [27] introduced a map display for an interactive overview visualization of surface data like WSS in cerebral analysis. They employed a 2D projection of the surface data along with the 3D aneurysm model, increasing the ease of use and minimizing mental effort. Gasteiger et al. [14] proposed an adaptive surface visualization to reduce occlusion and visual clutter when rendering flow and the enclosing vessel surface. They incorporated illustrative rendering techniques to ensure maximum visibility of the embedded flow visualization, whilst simultaneously enhancing shape and depth perception of the enclosing surface. Neugebauer et al. [26] presented an anatomy-guided exploration in cerebral aneurysms by using the vessel centerline and derived anatomic landmarks to ease the probe or seed plane placement. A focus-and-context approach, similar to the methods of Mattausch et al. [24], was presented by Gasteiger et al. [13] for the investigation of hemodynamic attributes. They introduced the FLOWLENS, which is a 2D lens to visualize a focus parameter (e.g., surface pressure) within the lens and a context parameter outside the lens.

Substantial work has been carried out to analyze and visualize blood flow using advanced flow visualization, illustrative rendering, map projections and lens-based interaction. Our primary goal is to detect and extract the inflow jet and impingement zone in cerebral aneurysm blood flow. While most of the related works deal with a visual explo-

ration of the flow behavior, they do not focus on an automatic detection of such qualitative hemodynamic characteristics. Our approach is inspired by line predicates, which analyze local streamline properties. Instead of evaluating Boolean functions we employ these properties to compute scalar fields on which we extract the inflow jet and impingement zone.

### 3 MEDICAL RESEARCH BACKGROUND

Improvements in medical imaging and an increased number of patient examinations have led to more incidental findings of unruptured intracranial aneurysms. Every unruptured aneurysm bears the risk of rupture with an annual rupture rate of 1% to 2%, a mortality rate in case of rupture of 40% to 50% and a morbidity rate of 10% to 20% [2]. The most common way to treat aneurysms is an endovascular procedure. One or more coils are placed in the aneurysm, often combined with a stent in the parent vessel to prevent the coils from dropping out. As a consequence, the turnover time of the blood in the aneurysm is increased and a thrombosis formation is initiated, which encapsulates the aneurysm from the blood circulation. The turnover time is a measure for the blood particle duration in the aneurysm sac and defined as the aneurysm volume divided by the aneurysmal inflow rate at the aneurysm neck. Every treatment, however, carries a risk of complication, especially during coil placement. The decision to treat an aneurysm has to be balanced against the risk of rupture. In cases of multiple aneurysms, the question arises which of them should be treated first [9]. Because prognosis of ruptures is still poor and depends not only on aneurysm morphology, biomedical researchers investigate the hemodynamics in the aneurysm and its influence in terms of aneurysm initiation, growth, and risk of rupture.

#### 3.1 Characterization of Flow in Cerebral Aneurysms

The analysis of flow data in cerebral aneurysms comprises quantitative flow parameters, such as WSS and speed, and qualitative flow characteristics. Examples of essential qualitative characteristics are the inflow jet, its impingement zone, or the grade of vorticity. Due to the complexity of quantitative and qualitative information, the analysis involves a visual exploration. Our approach is focussed on the detection and visualization of two qualitative flow characteristics: the *inflow jet* and its *impingement zone*, since these characteristics play a prominent role in the understanding of aneurysms. Qualitatively, they are described as follows [6]:

**Inflow Jet:** A flow structure that consists of parallel inflow with high speed compared to other parts in the aneurysm. The jet is evaluated as concentrated or diffuse, depending on its thickness and penetration depth into the aneurysm sac.

**Impingement Zone:** The region on the aneurysm wall, where the inflow jet is seen to impact the wall for the first time and to change its direction and/or disperse. The size of that region is either evaluated as large or small based on the ratio between the area of the impingement region and the area of the aneurysm.

Recent studies indicate that these two characteristics are associated with the risk of rupture [2, 6, 8, 25]. A concentrated inflow jet with a small impingement zone correlates to an increased WSS and bulge formation on the aneurysm, increasing the risk of a future rupture. Furthermore, the investigation includes changes of the spatial location and extent of both characteristics in terms of pre- and post-stenting as well as changes over time.

#### 3.2 Data Acquisition

Hemodynamic information in cerebral aneurysms is primarily obtained by CFD simulations. Only recently it became possible to measure flow in cerebral arteries with 4D Phase-Contrast MRI (4D PC-MRI) modality. However, the cerebral flow measurement is restricted to rare and expensive 7 Tesla MR scanners that provide the necessary spatial resolution to represent at least major cerebral arteries. CFD simulations of the blood flow are based on approximations with many assumptions that are difficult to verify. However, studies have shown

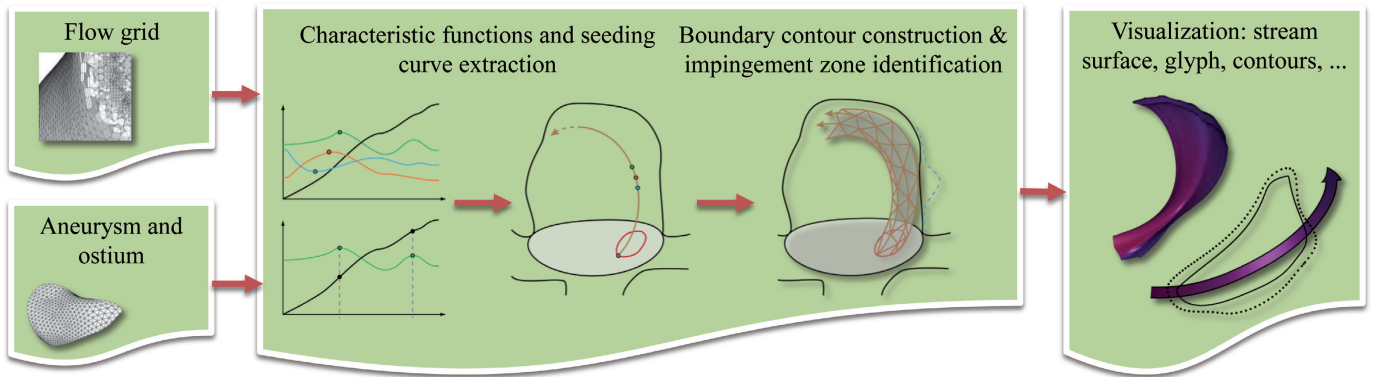


Fig. 1. Overview of the extraction approach: Based on the flow grid and the aneurysm ostium we seed streamlines at the ostium into the aneurysm. We identify several local line properties on the streamlines to compute a quality scalar field on the ostium. Given this scalar field we extract a seeding curve on the ostium, which is used to construct the boundary contour of the inflow jet. A second scalar field is computed on the aneurysm surface to indicate the impingement zone. Finally, we visualize both information expressively.

that image-based patient-specific CFD models are capable of reproducing the flow structures observed in vivo during angiographic examinations [7]. Furthermore, simulations enable to study the hemodynamics in different vessel geometries and to assess treatment options. Thus, we focus on simulated blood flow data and briefly present the data acquisition pipeline.

**Image Data Acquisition:** Clinical image data (CTA, MRA, or 3D rotational angiography) of the aneurysm morphology are acquired. Common clinical resolutions are up to  $512 \times 512 \times 140$  with a voxel size of  $0.35 \times 0.35 \times 0.9$  mm.

**Surface Reconstruction:** Based on the image data the vessel surface is reconstructed. This involves a segmentation of the aneurysm and parts of its parent vessel. Because of the high vessel-to-tissue contrast in the image data, often a simple thresholding segmentation followed by a connected component analysis is sufficient to separate the aneurysm and its parent vessel from the surrounding tissue. More advanced techniques, such as active shape models and deformable models, can be employed to minimize manual effort in cases of low vessel contrast in the image data [21]. Based on the segmented mask, the surface mesh of the aneurysm is reconstructed with Marching Cubes and optimized with respect to mesh quality necessary for the simulation process [32].

**Extraction of Anatomic Landmarks:** Neuroradiologists utilize anatomic landmarks, such as parent vessel centerlines and the ostium region, to describe aneurysm morphology. The ostium region is the contour around an aneurysm, which describes its neck. We extract these landmarks based on the reconstructed vessel surface. In particular, our approach employs the ostium surface, which is the surface triangulation of ostium contour and separates the aneurysm sac from its parent vessel. We utilize the approach of Neugebauer et al. [26] to automatically identify and reconstruct the ostium surface.

**Generating Simulated Flow Data:** Finally, the optimized vessel surface mesh is used for generating a volume mesh on which the subsequent CFD simulation is performed. The simulation model approximates the blood flow by the 3D Navier-Stokes equations for an incompressible Newtonian fluid with rigid walls. Boundary conditions, such as the inflow profile, were obtained from the literature or flow measurements [4].

#### 4 REQUIREMENT ANALYSIS

The localization of the impingement zone is directly related to the position and pathway of the inflow jet. Currently, neither a formal definition of the inflow jet exists nor a corresponding extraction of both characteristics is known. However, at least an informal description from Cebra et al. is available [5, 6]. This definition is not precise enough to enable a reproducible extraction that would be necessary in particular for comparisons. We subsequently define requirements that are derived from medical research papers and from discussions with

domain experts:

**Formalization:** A formalization of the target flow structures, namely the inflow jet and the impingement zone, is required. The formal characterization should reliably discriminate the target flow structures from any other structures. Formalization has to be exclusive in terms of a reliable detection of the inflow jet.

**Automatic and Robust Detection:** Based on the formalization, an automatic and robust detection approach is necessary to facilitate a reproducible detection. The approach should be free of parameters and robust with respect to noise, sampling, and discretization artifacts.

**Expressive Visualization:** A set of expressive visualization techniques is needed that conveys the location and character of the inflow jet and the impingement zone. The target structures must not be obscured and should be clearly recognizable. In order to reduce manual effort, carefully chosen default values should be provided.

#### 5 DETECTION OF THE INFLOW JET AND IMPINGEMENT ZONE

Our approach (see Fig. 1) to detect the inflow jet and the impingement zone is based on the assumption that the inflow jet is a *stream object*, which is bounded by a boundary contour  $C$ . This means that the boundary contour is a stream surface, which can be described by a closed seeding curve  $S$ :  $C$  is obtained by applying a numerical stream surface integration starting from  $S$ .

To find the boundary contour  $C$ , we have to solve two problems. Firstly, we have to define conditions for streamlines to be part of  $C$ . Secondly, we have to find a closed seeding curve  $S$  for starting the integration. Note that this problem does not have a unique solution: there are several seeding curves producing the same stream surface. To overcome this, we restrict ourselves to seeding curves on the inflow part of the ostium surface. Figure 2 illustrates the setup.

For the second problem, we collect local properties of a streamline to be part of the inflow jet. To define them, we use the relation between inflow jet and impingement zone. In fact, we assume that at a certain point of a streamline in the inflow jet comes close to the impingement zone. This means that a streamline of the inflow jet should contain locations where three properties are simultaneously fulfilled:

- A:** The point of the streamline should have a locally minimal distance to the aneurysm surface.
- B:** There should be a rapid change of flow direction.
- C:** There should be a strong change of flow speed, i.e., a strong magnitude of the acceleration of the velocity field.

Clearly, in general there is no streamline consisting of a point fulfilling A-C simultaneously. We have to come up with an approach to search for streamlines fulfilling A-C as much as possible. Given is a point  $\mathbf{x}_0$  on the ostium surface. From  $\mathbf{x}_0$  we integrate the streamline  $\mathbf{x}(t)$  with  $\mathbf{x}(0) = \mathbf{x}_0$ . We compute the following characteristic functions of  $\mathbf{x}(t)$ :

- $d(t)$  is the minimum distance of  $\mathbf{x}(t)$  to the aneurysm surface,

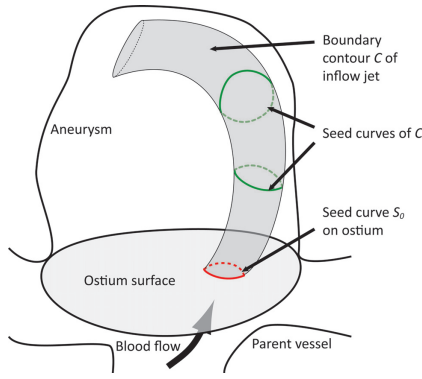


Fig. 2. Setup for computing the inflow jet: it is bounded by a contour surface  $C$ , which is a stream surface given by a closed seeding curve  $S_0$ . Different seed curves define the same stream surface. We focus on the seeding curve  $S_0$  on the ostium.

- $a(t) = \|\mathbf{a}(t)\|$  where  $\mathbf{a}(t) = \frac{\partial^2 \mathbf{x}}{\partial t^2}$  is the acceleration of the streamline,
- $c(t) = \frac{\|\dot{\mathbf{x}} \times \mathbf{a}\|}{\|\dot{\mathbf{x}}\|^3}$  is the curvature of the streamline where  $\dot{\mathbf{x}} = \frac{\partial \mathbf{x}}{\partial t}$  is the tangent vector of  $\mathbf{x}$ , and
- $l(t) = \int_0^t \|\dot{\mathbf{x}}(s)\| ds$  is the arc length of the streamline from  $\mathbf{x}_0$ .

Technically, the functions  $d, a, c$  are computed by precomputing the 3D scalar fields  $d(\mathbf{y}), a(\mathbf{y}), c(\mathbf{y})$  as

- $d(\mathbf{y})$  is the distance of a 3D point  $\mathbf{y}$  to the aneurysm surface.
- $a(\mathbf{y}) = \|\mathbf{J}(\mathbf{y}) \mathbf{v}(\mathbf{y})\|$  where  $\mathbf{v}$  and  $\mathbf{J}$  are velocity field and Jacobian at  $\mathbf{y}$ , respectively, and
- $c(\mathbf{y}) = \frac{\|\mathbf{v} \times \mathbf{a}\|}{\|\mathbf{v}\|^3}$  is the local streamline curvature at  $\mathbf{y}$ .

Then, we get  $d(t) = d(\mathbf{x}(t))$ ,  $a(t) = a(\mathbf{x}(t))$ , and  $c(t) = c(\mathbf{x}(t))$ . Furthermore,  $l(t)$  is computed by using the polygonal approximation of  $\mathbf{x}(t)$  resulting from the numerical integration. From the functions  $d, a, c$  we compute the following parameter values:

- $t_d$  is the smallest positive  $t$  where  $d(t)$  has a local minimum,
- $t_a$  is the smallest positive  $t$  where  $a(t)$  has a local maximum,
- $t_c$  is the smallest positive  $t$  where  $c(t)$  has a local maximum.

Before computing them, we employ a Gaussian smoothing on the streamline data values to reduce noise due to resampling artifacts. Figure 3 (left) gives an illustration. The parameter values  $d, a, c$  define the following characteristic points of the streamline:  $\mathbf{x}_d = \mathbf{x}(t_d)$ ,  $\mathbf{x}_a = \mathbf{x}(t_a)$ ,  $\mathbf{x}_c = \mathbf{x}(t_c)$ . Figure 3 illustrates this.

Now, we can characterize the inflow jet in the following informal way: The streamline  $\mathbf{x}(t)$  is part of the inflow jet if the points  $\mathbf{x}_d, \mathbf{x}_a, \mathbf{x}_c$  are close to each other (in arc length distance), and the points  $\mathbf{x}_d, \mathbf{x}_a, \mathbf{x}_c$  are not too far away from the seeding point  $\mathbf{x}_0$  (in arc length distance). We formalize this by the following quality function:

$$q(\mathbf{x}_0) = l_{a,c,d} \cdot (|l(t_a) - l(t_c)| + |l(t_c) - l(t_d)| + |l(t_a) - l(t_d)|), \quad (1)$$

with

$$l_{a,c,d} = \frac{1}{3} \cdot (l(t_a) + l(t_c) + l(t_d)).$$

Computing  $q$  on every point of the ostium surface gives a scalar field on the ostium. Note that isoline  $q = 0$  would give the ideal seeding curve, but it does not generally exist because no streamline needs to exist consisting of a point fulfilling **A-C** at the same position. Thus, setting a small threshold  $q = q_0$  gives the seeding curves  $S_0$  for the boundary contour. Throughout the paper we have chosen  $q_0 = q_{0.05}$ , with  $q_{0.05}$  as the five percent quantile of all values in  $q$ .

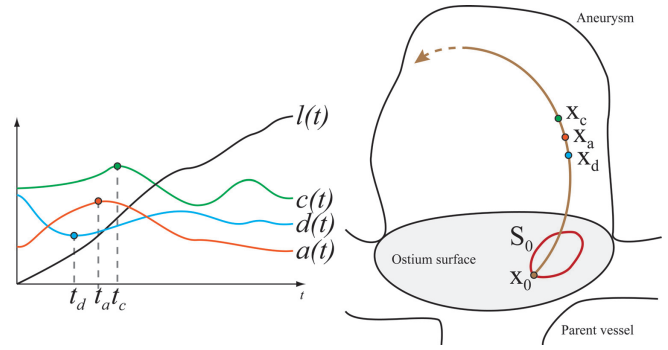


Fig. 3. The 4 characteristic functions of a streamline (left), together with their first extrema, (right) the corresponding points of the streamline.

### 5.1 Construction of the Inflow Jet Boundary Contour

The construction of the boundary contour is accomplished by numerical integration of the inflow jet seeding curve  $S_0$  in forward direction along the flow. For this, a criterion is required that indicates an appropriate stop of integration. The inflow jet disperses shortly after the impingement zone, associated with a rapid change of curvature (cf. Sec. 3). From there, the jet disperses in the rest of the aneurysm blood flow. Since the first local maximum of the curvature is assumed to be close to the impingement zone, we employ the second local maximum as stop criterion. This facilitates a sufficient length after the impingement zone. We formalize this as follows: first, the arc length  $l_{c_2} = l_{\mathbf{x}_0, \mathbf{x}_{c_2}}(\mathbf{x}(t))$  along each streamline  $\mathbf{x}(t)$  of the boundary contour is measured from the seeding point  $\mathbf{x}_0 \in S_0$  to the point  $\mathbf{x}_{c_2}$  being the second local maximum  $t_{c_2}$  of the curvature  $c(t)$ , illustrated in Figure 4. Second, the arc length of each streamline  $\mathbf{x}(t)$  of the boundary contour is restricted to the median  $l_s$  of the arc length values  $l_{c_2}$ , which yields the desired stop criteria:  $l_s = \text{median}(l_{c_2})$ . Finally, the numerical representation of the boundary contour is given by a triangulation of neighboring streamlines (see Fig. 4). Furthermore, for each contour vertex a pair of  $(u, v)$ -texture coordinates is assigned with  $u$  and  $v$  increasing around the boundary contour and along the streamline, respectively.

### 5.2 Indication of the Impingement Zone

With regard to the literature, the impingement zone depends on the inflow jet where it is seen to impact the aneurysm wall the first time, and where it is associated with a change of the flow direction (cf. Sec. 3). Hence, our approach uses property **B** again in order to compute a scalar field  $f$  for each point  $\mathbf{p}$  on the aneurysm surface that indicates the im-

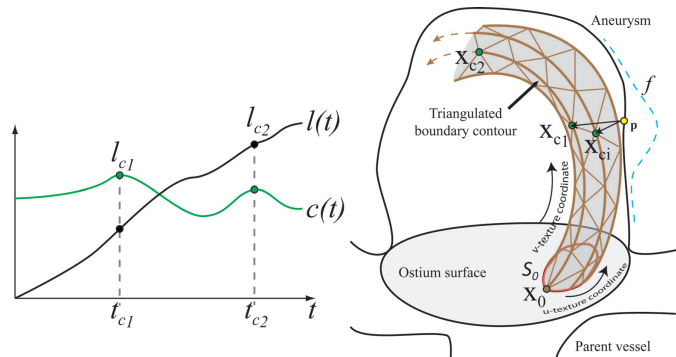


Fig. 4. Integration stop criteria: (left) the arc length and curvature functions of a streamline, together with the second maximum of the curvature, (right) the corresponding points of the streamline.

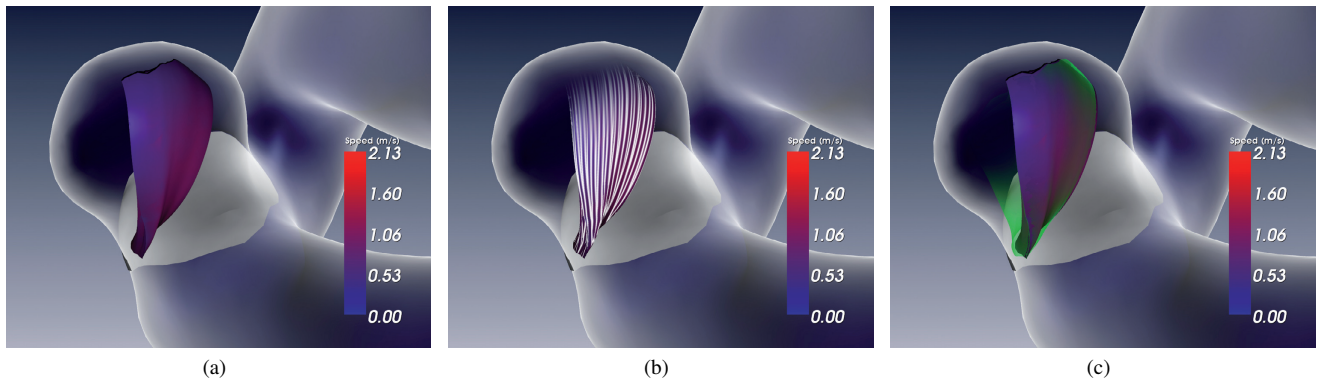


Fig. 5. The visualization styles of the inflow jet boundary surface: (a) color-coded surface shading, which is in (b) enhanced with surface stripes to convey surface shape. In (c) a second boundary surface indicates a safety margin visualized with Fresnel shading.

impingement zone, given by:

$$f(\mathbf{p}) = \frac{1}{n} \sum_{i=1}^n \|\mathbf{p} - \mathbf{x}_{c_i}\|, \quad (2)$$

with  $n$  being the number of available points  $\mathbf{x}_{c_i}$ ,  $i = 1, \dots, n$  (see Fig. 4). Formally speaking, the smaller  $f(\mathbf{p})$  is, the larger is the probability that the aneurysm surface point  $\mathbf{p}$  is part of the impingement zone. In Section 6.3, this scalar field is applied for a comprehensible impingement zone visualization.

## 6 VISUALIZATION OF HEMODYNAMIC CHARACTERISTICS

In this section, we provide several visualization techniques of the inflow jet boundary contour and the impingement zone. Additionally, the surface of the aneurysm and its parent vessel are illustrated as anatomical context in order to further support the interpretation of the presented visualization approaches. Our approach applies a ghosted view [14] to enhance the enclosing vessel surface while ensuring a maximum visibility of the embedded visualizations.

### 6.1 Visualization of the Inflow Jet Boundary Contour

The result of the inflow jet boundary contour construction is a stream surface based on the seeding curve  $S_0$ , given by the quality function  $q(\mathbf{x}_0)$  (cf. Eq. 1) and threshold  $q_0$ . Our approach depicts this surface with standard Phong shading and a color coding of the speed of the underlying blood flow field. A blue-to-red color mapping is used, since this is a familiar slow-to-fast color scale for physicians (see Fig. 5(a)). Inspired by illustrative integral surface renderings [17, 35] and hatching, our approach optionally provides surface stripes to enhance the surface shape and bending behavior of the inflow jet boundary (see Figure 5(b)). The stripes are procedurally generated in the fragment shader using the assigned  $(u, v)$ -texture coordinates from Section 5.1. Additionally, we ensure a uniform stripe density in screen space [11]. Since the inflow jet disperses after the impingement zone, the flow behavior becomes less predictable. To convey this, our technique provides a fade-out effect of the surface after it reaches the impingement zone. Thus, the start location corresponds to  $\mathbf{x}_{c_1}$  (property **B**), and we convert  $\mathbf{x}_{c_1}$  to the  $v$ -texture space. The opacity is linearly decreased for each surface point larger than the corresponding  $v$ -texture coordinate until it reaches the end of the surface. The fade-out effect can be seen in Figure 5(b), where it was added to the surface stripes visualization. To avoid misleading interpretations of this sharp boundary contour depiction, we provide a *safety margin* as second boundary contour around it. This boundary contour corresponds to  $q_0 = q_{0.1}$  with  $q_{0.1}$  as the ten percentile of all values in  $q$ . We visualize this boundary contour with a fuzzy-like surface rendering by modulating the surface opacity with an approximation of the Fresnel reflection, depicted in Figure 5(c). The Fresnel opacity  $o$  can be expressed by  $o = 1 - (\mathbf{n} \cdot \mathbf{e})^r$ , where  $\mathbf{n}$  is the surface normal,  $\mathbf{e}$  is the view vector, and  $r$  is an edge fall-off parameter ( $r \geq 0$ ).

### 6.2 Visualization of the Inflow Jet as Glyph

In addition to a solid visualization of the inflow jet boundary contour our technique provides a more simplified description of it. Inspired by illustrative flow drawings in anatomical textbooks, we use an arrow glyph to depict the jet. The glyph geometry is view-aligned and points along the average direction of the inflow jet boundary surface. Additionally, we use a halo rendering at the glyph borders to highlight the glyph geometry from its background. The entire glyph is shown in Figure 6(a) and corresponds to the inflow jet presented in Figure 5. The glyph geometry itself is based on the geometric centerline generated by averaging the boundary contour streamlines. The resulting line is depicted with view-aligned quads similar to the illustrative line rendering approach presented in Everts et al. [10]. We optionally provide the same speed color encoding as for the boundary surface.

### 6.3 Visualization of the Impingement Zone

For the depiction of the impingement zone we employ the scalar field on the aneurysm surface computed by the quality function  $f(\mathbf{p})$ , defined in Eq. 2. A trivial visualization technique would be to highlight such surface points which consist of the minimum value  $f(\mathbf{p})$ . Since only a few points would fulfill this condition, this kind of technique poorly conveys the spatial extension of the impingement zone. Therefore, we propose two more expressive visualization techniques of the impingement zone. First, we use an iso-contouring on the scalar field similar to the extraction of the seeding curve  $C$  by choosing a threshold lower than  $f = f_{0.05}$ . Additionally, we also provide a *safety margin* contour line by using  $f = f_{0.1}$  and depict it with a stippling pattern. Note that  $f_b$ ,  $b \in \mathbb{R}$  is the  $b$  percentile of all values of  $f$ . The final result can be seen in Figure 6(b), where the contour lines were smoothed with a spline interpolation to reduce sampling artifacts due to the linear interpolation of the iso-contouring. Furthermore, this sparse representation can be used as an overlay for several hemodynamic surface attributes like pressure or wall shear stress to support the correlation

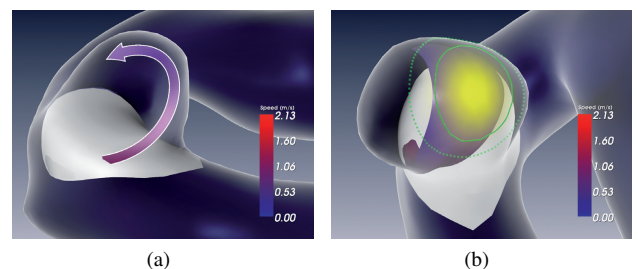


Fig. 6. (a) Depiction of the inflow jet by an arrow glyph, (b) contour rendering of the impingement zone and its safety margin. Within the contour the quality function is mapped to opacity (yellow).

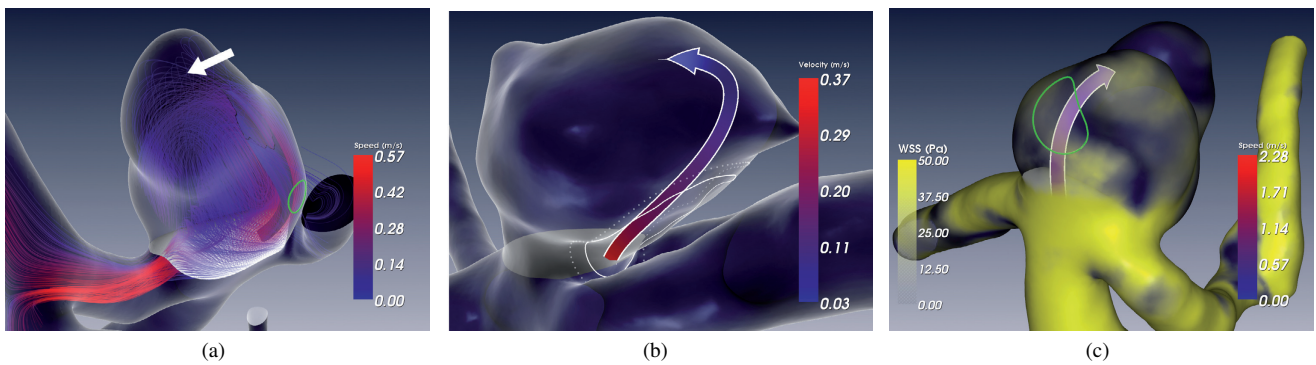


Fig. 7. Depiction of extracted inflow jets and impingement zones for three different datasets. In (a) a visualization of the color-coded inflow jet boundary contour enclosed by the inflow streamlines is shown. The white arrow points to a known rupture location, which is apart from the indicated impingement zone (green). The color-coded inflow jet glyph is used in (b) with an impingement zone near to the ostium. A second zone could occur at the dome point. The correlation between inflow jet (glyph) and impingement zone (green contours) with wall shear stress (WSS) distribution is shown in (c). The magnitude of WSS is mapped to opacity.

between these attributes and the impingement zone (see Fig. 7(c)).

The second visualization technique for the impingement zone consists of an opacity mapping of the scalar field. We map the maximum scalar value to fully opaque and the scalar value corresponding to  $f = f_{0.1}$  to fully transparent. We blend a surface color linearly between both values. This is shown in Figure 6(b) with a yellow surface color. In contrast to the contour rendering, the opacity mapping conveys different levels of closeness to the underlying relevant inflow jet regions. Note that this can also be accomplished by multiple contour lines lower than  $f = f_{0.05}$ .

## 7 APPLICATION AND EVALUATION

In order to evaluate our approach, we employed five steady flow datasets (as well as their ostiums and aneurysm surfaces), which were derived from CFD simulations. The resolution of the flow grids ranges from 181,000 to 2,308,785 volume elements (tetrahedra and prisms). On our prototypic system, the preprocessing time of the datasets ranges from 20 to 120 sec on a mid-class desktop computer (Core 2 Duo 3.16GHz, 8GB RAM, nVidia GeForce 9800 GT), depending on the resolution of the dataset. The preprocessing includes dataset loading, tracing the inflow streamlines, and computing the scalar fields  $d(\mathbf{y})$ ,  $a(\mathbf{y})$ , and  $c(\mathbf{y})$ . The computation of  $q(\mathbf{x}_0)$  and  $f(\mathbf{p})$  (recall Eq. 1 and Eq. 2), the extraction of the seeding curve, the construction of the inflow jet boundary contour and glyph as well as the generation of the contour lines are accomplished in 7 to 20 seconds for each dataset. The visualization techniques described in Section 6 and their adjustments can be performed at interactive rates. The approach is embedded in the prototyping environment MEVISLAB and implemented in C++, supported by OpenGL, GLSL, and the Visualization Toolkit (VTK).

The whole extraction process of the inflow jet and impingement zone is accomplished automatically. The relevant parameters consist of the iso-values for extracting the inflow jet boundary contour  $S$  on the ostium (see Sec. 5) and for extracting the impingement zone (see Sec. 5.2). Since we derive these values statistically from the corresponding scalar fields, no user adjustments are necessary.

In Figure 7, a series of three CFD datasets with their extracted inflow jets and impingement zones are shown. The inflow jet in Figure 7(a) is depicted with the color-coded stream surface visualization enclosed by the inflow streamlines. The impingement zone and its safety margin is indicated by the green contour rendering. For this dataset, a former rupture location is known and highlighted with a white arrow by a domain expert. An interesting observation is the difference between the impingement zone and the rupture location. Even the manually adjusted impingement zones by the domain experts (see Sec. 7.1) show this difference. The correlation between impingement zone and the potential location of a rupture is still unclear and needs further investigation. However, the small size of the extracted

impingement contour correlates to the observation of recent studies that small impingement zones are associated with an increased risk of rupture (see Sec. 3).

In Figure 7(b) the inflow jet is illustrated by the color-coded glyph geometry to depict the average direction and speed of the stream surface. The glyph indicates a straight inflow of the jet and a strong curvature at the aneurysm dome with low speed. Our approach indicates the impingement zone near to the ostium because the first local curvature maxima of the boundary streamlines are located there. Furthermore, for this particular location the flow seems to hit the aneurysm surface with high speed. However, a second impingement zone could occur at the dome point of the aneurysm where the inflow jet consists of a high curvature. To support the investigation of the correlation between wall shear stress (WSS) and impingement zone, the hemodynamic structures are shown in Figure 7(c). The WSS is encoded on the front faces of the aneurysm with a yellow color map where the WSS magnitude is mapped to the opacity. The inflow jet is indicated by the glyph visualization and the impingement zone by the green contour rendering. The visualization shows an increased WSS distribution at the neck of the aneurysm but not within the impingement zone contour. Thus, the observation of Cebal et al. [5], who stated an increased WSS distribution at the impingement zone, could not be confirmed for this dataset.

### 7.1 Evaluation

The evaluation of our approach considers quantitative and qualitative assessments of five representative datasets ( $D_1$ - $D_5$ ). Three biomedical researchers and three neuroradiologists participated as domain experts in the evaluation. Two of the three biomedical researchers are experts in CFD simulations and strongly involved in blood flow simulation for cerebral aneurysms. One biomedical researcher is specialized in 4D PC-MRI blood flow measuring and its evaluation with advanced flow tools like EnSight. The neuroradiologists treat cerebral aneurysms regularly. Additionally, two of the three physicians are involved in clinical research on the investigation of the risk of rupture or heart diseases due to pathological blood flow behavior. The evaluation comprises a robustness analysis of the inflow jet boundary surface extraction, a qualitative comparison between the automatically and manually extracted inflow jet and impingement zone as well as an informal user feedback of the employed visualization techniques for both hemodynamic characteristics.

#### 7.1.1 Robustness

The extracted inflow jet boundary surface is based on the boundary contour determined on the ostium's surface. Thus, we evaluate the robustness and sensitivity of the boundary surface extraction w.r.t. a variation of the boundary contour and the ostium's surface as seeding structure. In order to measure the robustness, we investigated the variation of the input: the boundary contour is linearly scaled to its

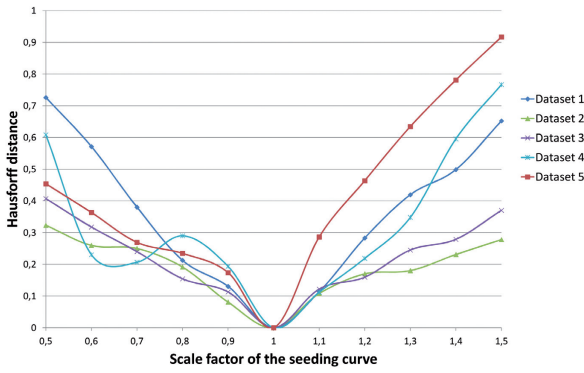


Fig. 8. Robustness in terms of the seeding contour variation and the Hausdorff distances between resulting boundary contours.

double and half size. We measure the Hausdorff distances [28] from the original inflow jet boundary surface to the inflow jet boundary surface which is determined subsequently to the mentioned variation. This has been conducted for the four datasets. The distance results are shown in Figure 8: A strong sensitivity would lead to rapid and large jumps within the Hausdorff distances caused by strong differences in the shape of the resulting inflow jet boundary surfaces. However, the diagram shows that the distances (approximately) grow linearly with the considered variation. This behavior corresponds to a low sensitivity and affirms the robustness of the approach.

### 7.1.2 Qualitative Comparison of the Inflow Jet

Since there is no gold standard for a *real* inflow jet, we qualitatively compare the results of our automatic detection approach with the results that are adjusted by the domain experts. As a consequence, exploration methods are required, which enable the experts to interactively specify an inflow jet. In practice, however, the investigation of the inflow jet is novel and no standard techniques exist to precisely extract the inflow jet. Thus, we provide a framework that consists of several visual exploration techniques including color-coded streamlines, cross-section planes, and speed isosurfaces. These techniques are also chosen by Cebra et al. [5, 6] and seem to be accepted in the domain-specific literature. The participants were asked to perform four tasks to specify an inflow jet in each dataset and to compare it to the automatically detected one. For each of the following tasks the aneurysm surface with its ostium was provided and the participants could fully interact (zoom and rotate) with the 3D scene:

**Task 1:** Specification of the inflow jet streamlines by filtering the inflow streamlines according to their color-coded speed. The streamlines are seeded on the ostium in forward direction and the filtering is performed by adjusting a speed threshold. Each streamline, which has at least one vertex above the threshold, is removed. For further comparison we extract a concave contour on the ostium's surface based on the adjusted inflow jet streamline bundle. This contour is considered as an approximated boundary contour of the manually adjusted inflow jet.

**Task 2:** Specification of a speed isosurface of the inflow jet, which starts at the ostium and ends up at the thought impingement zone. To generate the isosurface, participants are able to adjust an isovalue of the speed and get a visual feedback of the resulting isosurface.

**Task 3:** Alignment of a cross-section plane, which describes a *core* cross-section through the inflow jet. The plane is color-coded with the probed speed values and can be adjusted by a widget, which has handles to translate or rotate the plane in arbitrary directions. Additionally, the participants can turn on/off the inflow jet streamlines and speed isosurfaces they adjusted before to get hints about the spatial orientation of the jet.

**Task 4:** Evaluation of the manually specified and automatically extracted inflow jets by answering the following questions after **tasks 1-3** were finished:

**Q1:** Did you overestimate or underestimate the adjusted inflow jet in task 1 and task 2?

**Q2:** Which of the inflow jets do you judge to be more accurate, the automatically or manually extracted one, and why? For this question, the participants were shown their adjusted inflow jet streamline bundle and the automatically extracted inflow jet stream surface for each dataset. Additionally, they could embed the adjusted cross-section plane and speed isosurface for further hints.

**Q3:** Did you feel you have been limited by the provided framework to specify the inflow jet?

For the qualitative comparison between the automatically detected and the manually adjusted inflow jets we compare the following two results for each dataset: (1) The shape and location of the inflow jet boundary contours on the ostium resulting from **task 1** with the boundary contour  $C$  of Section 5, and (2) the location of the cross-section planes with respect to the inflow jet stream surface of Section 5.1. We expect for comparison (1) an intersection of the contour  $C$  with the manually extracted contours and for comparison (2) an intersection of the cross-section planes with the stream surface. The more the intersections are equal in shape and location, the more the automatically and manually extracted inflow jets are correlated to each other.

In Figure 9, the comparison is shown. The results of the participants and the automatic approach are labeled with different colors. In the top row of Figure 9 the seeding curves on the ostium are shown, where several observations can be made. There exists an intersection between the manually extracted seeding curves, but their individual sizes vary among the datasets. It follows that there is some significant overlap among the participants in terms of the inflow jet streamline bundle, but also that some of the participants seem to specify the inflow jet in varying degrees of *sharpness*. Furthermore, it can be seen that the automatically extracted seeding curve is embedded in the intersection of the manually extracted curves in each dataset. Thus, our approach detects the location of the inflow jet relatively close to the manually specified inflow jet streamline bundles. For two datasets ( $D_4$ ,  $D_5$ ) the automatically extracted curve is located at the center of intersections between the manual curves, which implies a strong correlation between the boundary contour and the *core* of the adjusted inflow jet streamline bundles. However, there are some differences in terms of the shape and location. First, in three datasets ( $D_1$ - $D_3$ ) the seeding curve is located more or less at the edge of the intersection, which corresponds to a moderate correlation to the manually specified inflow jet streamlines. Second, in almost each dataset the seeding curve is smaller and more circular compared to the manually extracted ones, which are more elongated. This implies that our approach underestimates the inflow jet.

The bottom row in Figure 9 shows the comparison between the cross-section planes and the color-coded inflow jet boundary contour. Similar to the manually adjusted inflow jet streamline bundles, the differences of the planes' locations and alignments vary between the participants. Except for dataset  $D_2$ , however, the planes' intersections seem to be close to each other, which implies a moderate to strong correlation in terms of the inflow jet core direction. Based on these intersections, it can be seen that the boundary contour in datasets  $D_1$ ,  $D_4$ , and  $D_5$  is also part of the corresponding inflow jet core. For dataset  $D_2$  the boundary contour is close to the intersections and for dataset  $D_3$  the correlation to the inflow jet core seems to be weak.

### 7.1.3 Qualitative Comparison of the Impingement Zone

The next part of the evaluation consists of a comparison of the automatically extracted impingement zone with the manually indicated impingement zones by the participants. Since an impingement zone is based on the underlying inflow jet, there is also no gold standard for such an aneurysm surface region. Thus, we compare the impingement zones qualitatively like the inflow jets before. We extended our framework by a surface drawing tool and asked the participants to perform the following tasks:

**Task 5:** Specification of the impingement zone by drawing a contour on the aneurysm surface where the inflow jet seems to hit the

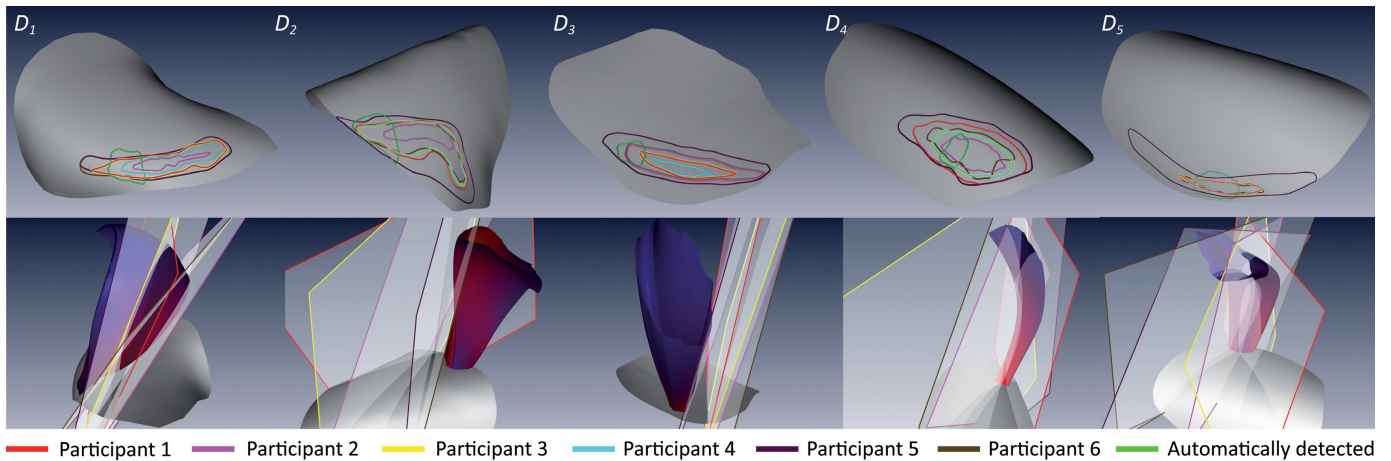


Fig. 9. Qualitative comparison of the inflow jet between the automatically and manually extracted inflow jet: (top) resulting seeding curves on the ostium, (bottom) cross-section planes related to the extracted boundary contours. Each column represents the same dataset.

surface. For this task, the participants were shown their adjusted and color-coded inflow jet streamline bundles from Section 7.1.2 enclosed by the aneurysm surface visualization. Additionally, they were able to embed their cross-section planes as a further spatial hint of the inflow jet specification. Initially, a spline contour on the aneurysm surface was shown with four handles. The participants were able to move the handles on the surface, to insert new handles or to remove them. During the interaction, the spline contour has been adapted and was located on the aneurysm surface.

**Task 6:** Evaluation of the manually specified and automatically extracted impingement zone by answering three questions (Q4-Q6) after task 5 was finished. The questions Q4 through Q6 were the same as questions Q1 through Q3 in task 4, but with replacing “inflow jet” by “impingement zone”.

For the qualitative comparison, we use the extracted impingement contour of our approach and compare its shape as well as its location with the manually indicated contours. We expect an intersection of both contour types. The more the intersections are equal in shape and location, the more the automatically and manually extracted impingement zone contours are correlated to each other. In Figure 10, the qualitative comparison is shown where the results of the participants and the automatic approach are labeled with the same color as for the inflow jet comparison in Figure 9. In addition to the impingement zone contours the automatically extracted inflow jet boundary contour is embedded as spatial hint for its corresponding impingement zone contour. Similar to the comparison of the inflow jet, several observations can be made. In terms of the intersection between the automatically and manually indicated impingement contours, a moderate to strong correlation can be seen for three datasets ( $D_2$ ,  $D_4$ , and  $D_5$ ). For the other two datasets, the intersection correlates weak in  $D_1$  and is empty in  $D_3$ , respectively. Contour size and shape are similar in three datasets ( $D_1$ ,  $D_2$ ,  $D_5$ ), but smaller and more circular in datasets  $D_3$  and  $D_4$ . However, an interesting observation is the relatively high inter-personal variance in terms of the contour size, shape, and location. It seems that the participants have different associations between inflow jet and impingement zone, which results in using different visual information to specify the impingement zone.

#### 7.1.4 Visualization Techniques

Besides the qualitative comparison, the participants were asked to evaluate the presented visualization techniques described in Section 6. For all techniques, the participants were able to interact with the scene. First, we considered the inflow jet surface depiction. All respondents stated that the visualization of the inflow jet as color-coded stream surface is comprehensible and that the color scale is reasonable. The additional safety margin was positively assessed, since it avoids a binary assessment of the inflow jet shape and extent. The stripe overlay

supports the shape perception in general, but its value depends on the grade of the surface twisting and bending. For a more helical and bended surface shape, the stripes were assessed expressive as for a more laminar and even oriented inflow jet surface. Thus, the surface stripes should be provided optionally. The fade-out effect of the stream surface after the impingement zone was rated as not necessary, since the sharp end of the inflow jet surface is assumed to be more reasonable in terms of the jet’s spatial extent. The next part of visualization evaluation addressed the inflow jet glyph. All participants appreciated the simplicity of the glyph. One participant suggested to use that description as an overview visualization at the beginning of the inflow jet investigation. For a more detailed view, however, the boundary contour was preferred, especially with respect to the shape and spatial extent of the inflow jet. Notably, one neuroradiologist rated the glyph depiction as not worthy. In contrast to this, one biomedical expert valued the glyph as helpful to identify the main inflow jet behavior, but it should be enclosed with the safety margin visualization to get an impression of the spatial extension.

Finally, we evaluated the visualization of the impingement zone. All participants appreciated the contour line depiction. One participant suggested to provide an opaque rendering of the contour interior optionally to indicate the region more prominently. He agreed that this would lead to an occlusion of the underlying flow information. However, he considered this not as disadvantage if the investigation focus would be on the impingement zone. The additional safety margin contour was also evaluated positively and should always be provided with the original impingement zone contour. In terms of the opacity encoding of the scalar field  $f$  the participants rated this visualization as reasonable to identify aneurysm surface regions with different relevances to the impingement zone. Similar to opaque rendering of the contour interior mentioned above, a participant pointed out the caused occlusion problem and suggested to try multiple contour lines instead.

## 7.2 Discussion

The qualitative comparison of the inflow jets and impingement zones allows us to draw some conclusions that are discussed in the following. For this discussion, we incorporate both the answers of the participants for the questions they were asked in task 4 and task 6 as well as their feedback during the evaluation. First, we address the comparison of the inflow jet. Although the domain experts stated to have an intuitive understanding of an inflow jet, their manual adjustments show a significant degree of variation among each other. On one side, they mostly agreed in adjusting the core of the inflow jet, but on the other side they defined the extension of the jet differently large. Five out of six domain experts stated that they probably overestimated the inflow jet streamline bundles and one expert declared to adjust the streamlines neither overestimated nor underestimated (Q1). Compared to the

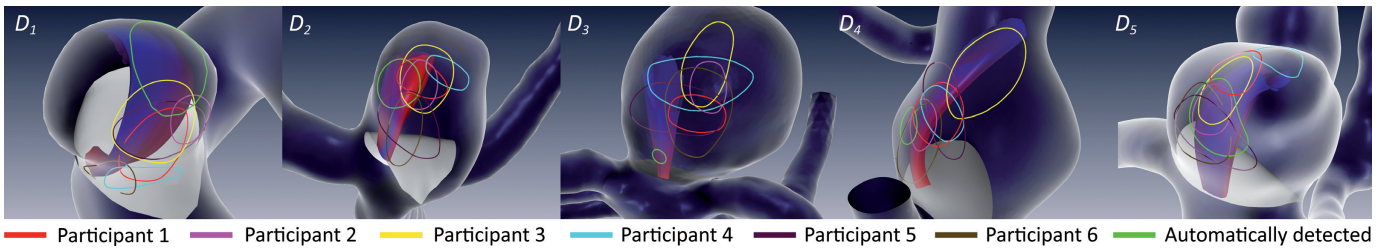


Fig. 10. Qualitative comparison of the impingement zones between the automatically extracted and manually specified regions by the participants.

domain experts our approach underestimated the inflow jet, since the shape of the underlying seeding curve  $S_0$  is always smaller than the seeding curves derived from the participants. However, the curve  $S_0$  is mostly placed in the intersection of all manually extracted seeding curves, and in three out of five datasets ( $D_1$ ,  $D_4$ , and  $D_5$ ) the resulting inflow jet boundary contour is located close to the manually defined inflow jet core. This observation was also considered by the participants in terms of judging the accuracy (Q2). They stated that for two datasets ( $D_4$ ,  $D_5$ ) the automatically extracted inflow jet is more accurate since the boundary contours comprise the inflow jet core more *sharp* compared to their specified streamline bundles. Furthermore, the lengths of the two boundary contours were assessed as sufficiently long enough after the impingement zone. For one dataset ( $D_1$ ), the resulting boundary contour was rated as at least accurate as the manually specified streamline bundles because of its closeness to the inflow jet core and its reasonable inflow behavior into the aneurysm. However, for two datasets ( $D_2$ ,  $D_3$ ), the manually adjusted streamline bundles were rated to be more accurate for two reasons: First, the stream surfaces were apart from the inflow jet core specification and more located at the edge of the streamline bundles. Second, the resulting boundary contour was assessed as too short and not reaching the impingement zone indicated by the adjusted streamline bundles. It seems that our stop criterion for the stream surface was too sensitive for these datasets (recall Sec. 5.1). Finally, the provided framework to specify the inflow jet was considered flexible enough in general (Q3). An interesting feedback was that some participants assessed the cross-section plane as not appropriate in some datasets to locate the inflow jet core. Due to the complexity of the jet course indicated by the adjusted streamline bundle, only parts of the core could be covered with the plane. Instead, a more deformable surface was desired. Fortunately, our detection approach might provide such a complex shape of the inflow jet. The underestimation of the inflow jet is caused by the quality threshold parameter  $q_0$ , which influences the size and shape of the seeding curve  $S_0$ . Since we use a threshold  $q_0$  less than the five percentile of all  $q$  as an established statistical measure, the resulting seeding curves were restricted to a small region of the ostium surface, which obviously leads to the underestimation. It follows that a less restrictive quality threshold  $q$  is more appropriate as the initial one.

The qualitative comparison of the impingement zone reveals several insights and conclusions. Four participants stated that they overestimated the impingement zones and two participants underestimated it (Q4), but all agreed about not being limited by adjusting the impingement zone (Q6). In terms of the accuracy between the automatically and manually specified impingement contour (Q5) an interesting discussion occurred. During the evaluation, the participants were aware that they have no clear definition of an impingement zone. Intuitively, they considered the magnitude of streamline curvature and the color-coded speed as visual hints to identify the impingement zone, but they preferred the curvature more. However, for some datasets they were unsure and would identify two impingement zones ( $D_1$ ,  $D_3$ ): One zone would be located at the aneurysm wall near to the ostium where the jet seems to hit the wall with high speed but low curvature. The other zone would be near the dome point where the curvature is obviously high but the speed is low, which is unlikely for an *impingement* behavior. Based on this experience and having in mind that the automatically extracted impingement zone contours rely on the streamline curvature,

the participants rated four datasets ( $D_1$ ,  $D_2$ ,  $D_3$ ,  $D_5$ ) at least as good as their impingement zone. The correlation between contour size and location with the underlying streamline curvature was reasonable and appropriate. Dataset  $D_3$  could also be meaningful because the automatically detected impingement zone is located at a region where the decreasing of speed seems to be high. Note: for that case, the first local curvature maximum correlates also with a high magnitude of acceleration. Thus, it could be worth to integrate the magnitude of acceleration into the impingement zone detection with different weighting. Later, multiple suggestions for the impingement zone could be provided depending on the weighting between curvature and acceleration. Finally, it seems that for some cases (e.g.,  $D_3$ ) the first local maximum of the curvature is not sensitive enough to ensure an appropriate inflow jet length with a subsequent impingement zone indication. It is reasonable that noise might influence the topology of, e.g., the curvature property (or other line properties) and that is the reason why we apply a noise smoothing (see Sec. 5). Nevertheless, for strong noise in the data it might be necessary to apply more sophisticated noise handling strategies, such as persistence-based [36] or scale-space-based approaches [30], which are directly related to future work.

## 8 CONCLUSIONS AND FUTURE WORK

Qualitative hemodynamic characteristics like inflow jet and its impingement zone play an important role for the investigation of rupture risk in cerebral aneurysms. We presented an approach to automatically extract both characteristics. In contrast to a manual extraction, our approach is novel in this field of application and yields reproducible results. Based on the literature and discussions with domain experts, we derived local streamline properties and used them for a formalization of the extraction process. We provided several visualization techniques to depict the inflow jet and impingement zone.

The qualitative comparison with six domain experts showed reasonable results for both characteristics. It could be shown that for three out of five datasets the automatically extracted inflow jet was rated as more accurate compared to the manually specified one, and that for four out of five datasets the corresponding impingement zones were meaningful. However, the evaluation also showed a high interpersonal variance in the specification of both characteristics. Overall, the domain experts stated that the specification is often subjective and based on different associations between inflow jet and impingement zone. This confirms the need for an automatic detection approach to gain reproducibility. For future work, the formalization can be extended with additional properties, which may improve the detection approach.

## ACKNOWLEDGMENTS

The authors would like to thank Uta Preim (Hospital Magdeburg, Germany), Cordula Scherlach (University Hospital Magdeburg, Germany), Daniel Stucht (Institute of Biomedical Magnetic Resonance, University Magdeburg, Germany) and Philipp Berg (Institute of Fluid Mechanics and Thermodynamics, University Magdeburg, Germany) for participating in the evaluation and providing their valuable feedback. Furthermore, we would like to thank the anonymous reviewers for their constructive comments as well as Fraunhofer MEVIS Bremen, Germany, for providing the prototyping platform MeVisLab.

## REFERENCES

- [1] S. Appanaboyina, F. Mut, R. Löhner, C. Putman, and J. Cebral. Computational Fluid Dynamics of Stented Intracranial Aneurysms Using Adaptive Embedded Unstructured Grids. *Numerical Methods in Fluids*, 57(5):475–493, 2008. 1
- [2] M. I. Baharoglu, C. M. Schirmer, D. A. Hoit, B.-L. Gao, and A. M. Malek. Aneurysm Inflow-Angle as a Discriminant for Rupture in Side-wall Cerebral Aneurysms Morphometric and Computational Fluid Dynamic Analysis. *Stroke*, 41(7):1423–1430, 2010. 2
- [3] S. Born, M. Pfeifle, M. Markl, and G. Scheuermann. Visual 4D MRI Blood Flow Analysis With Line Predicates. In *Proc. IEEE Pacific Visualization*, pages 105–112, 2012. 2
- [4] J. R. Cebral, M. A. Castro, S. Appanaboyina, C. M. Putman, D. Milan, and A. F. Frangi. Efficient Pipeline for Image-Based Patient-Specific Analysis of Cerebral Aneurysm Hemodynamics: Technique and Sensitivity. *IEEE Transaction on Medical Imaging*, 24(4):457–467, 2005. 3
- [5] J. R. Cebral, F. Mut, J. Weir, and C. M. Putman. Association of Hemodynamic Characteristics and Cerebral Aneurysm Rupture. *American Journal of Neuroradiology*, 32(2):264–270, 2011. 1, 3, 6, 7
- [6] J. R. Cebral, F. Mut, J. Weir, and C. M. Putman. Quantitative Characterization of the Hemodynamic Environment in Ruptured and Unruptured Brain Aneurysms. *American Journal of Neuroradiology*, 32(1):145–151, 2011. 1, 2, 3, 7
- [7] J. R. Cebral, R. Pergolizzi, and C. M. Putman. Computational Fluid Dynamics Modeling of Intracranial Aneurysms: Qualitative Comparison with Cerebral Angiography. *Academic Radiology*, 14(7):804–813, 2007. 3
- [8] J. R. Cebral, M. Sheridan, and C. M. Putman. Hemodynamics and Bleb Formation in Intracranial Aneurysms. *American Journal of Neuroradiology*, 31(2):304–310, 2010. 2
- [9] I. Chatziprodromou, V. D. Butty, V. B. Makhijani, D. Poulidakos, and Y. Ventikos. Pulsatile Blood Flow in Anatomically Accurate Vessels with Multiple Aneurysms: A Medical Intervention Planning Application of Computational Hemodynamics. *Flow, turbulence and combustion*, 71(1):333–346, 2003. 2
- [10] M. H. Everts, H. Bekker, J. B. Roerdink, and T. Isenberg. Depth-Dependent Halos: Illustrative Rendering of Dense Line Data. *IEEE TVCG*, 15(6):1299–1306, 2009. 5
- [11] B. Freudenberg, M. Masuch, and T. Strothotte. Real-Time Half-toning: A Primitive For Non-Photorealistic Shading. In *Proc. Eurographics workshop on Rendering*, pages 227–232. Eurographics Association, 2002. 5
- [12] H. Garcke, T. Preußner, M. Rumpf, A. C. Telea, U. Weikard, and J. J. V. Wijk. A Phase Field Model for Continuous Clustering on Vector Fields. *IEEE TVCG*, 7(3):230–241, 2001. 2
- [13] R. Gasteiger, M. Neugebauer, O. Beuing, and B. Preim. The FLOWLENS: A Focus-and-Context Visualization Approach for Exploration of Blood Flow in Cerebral Aneurysms. *IEEE TVCG*, 17(12):2183–2192, 2011. 2
- [14] R. Gasteiger, M. Neugebauer, C. Kubisch, and B. Preim. Adapted Surface Visualization of Cerebral Aneurysms with Embedded Blood Flow Information. In *Proc. VCBM*, pages 25–32, 2010. 2, 5
- [15] E. Heiberg, T. Ebbens, L. Wigström, and M. Karlsson. Three-Dimensional Flow Characterization Using Vector Pattern Matching. *IEEE TVCG*, 9(3):313–319, 2003. 2
- [16] A. Hennemuth, O. Friman, C. Schumann, J. Bock, J. Drexler, M. Markl, and H.-O. Peitgen. Fast Interactive Exploration of 4D MRI Flow Data. In *Proc. SPIE Medical Imaging*, 2011. 2
- [17] M. Hummel, C. Garth, B. Hamann, H. Hagen, and K. I. Joy. Iris: Illustrative Rendering for Integral Surfaces. *IEEE TVCG*, 16(6):1319–1328, 2010. 5
- [18] A. Kuhn, D. J. Lehmann, R. Gaststeiger, M. Neugebauer, B. Preim, and H. Theisel. A Clustering-based Visualization Technique to Emphasize Meaningful Regions of Vector Fields. In *Vision, Modeling, and Visualization*, pages 191–198. Eurographics Association, 2011. 2
- [19] R. S. Laramée, G. Chen, M. Jankun-Kelly, E. Zhang, and D. Thompson. Bringing Topology-Based Flow Visualization to the Application Domain. In H.-C. Hege, K. Polthier, and G. Scheuermann, editors, *Topology-Based Methods in Visualization II*, Mathematics and Visualization, pages 161–176. Springer, 2009. 2
- [20] R. S. Laramée, H. Hauser, L. Zhao, and F. H. Post. Topology-Based Flow Visualization, The State of the Art. In H. Hauser, H. Hagen, and H. Theisel, editors, *Topology-based Methods in Visualization*, Mathematics and Visualization, pages 1–19. Springer, 2007. 2
- [21] D. Lesage, E. D. Angelini, I. Bloch, and G. Funka-Lea. A Review of 3D Vessel Lumen Segmentation Techniques: Models, Features and Extraction Schemes. *Medical Image Analysis*, 13(6):819–845, December 2009. 3
- [22] M. Markl, F. Chan, M. Alley, K. Wedding, M. Draney, C. Elkins, D. Parker, R. Wicker, C. Taylor, R. Herfkens, and N. Pelc. Time-Resolved Three-Dimensional Phase-Contrast MRI. *Journal of Magnetic Resonance Imaging*, 17(4):499–506, 2003. 2
- [23] M. Markl, A. Harloff, T. A. Bley, M. Zaitsev, B. Jung, E. Weigang, M. Langer, J. Hennig, and A. Frydrychowicz. Time-Resolved 3D MR Velocity Mapping at 3T: Improved Navigator-Gated Assessment of Vascular Anatomy and Blood Flow. *Magnetic Resonance Imaging*, 25(4):824–831, 2007. 1
- [24] O. Mattausch, T. Theußl, H. Hauser, and E. Gröller. Strategies for Interactive Exploration of 3D Flow Using Evenly-Spaced Illuminated Streamlines. In *Proc. SCCG*, pages 230–241, 2003. 2
- [25] H. Meng, Z. Wang, Y. Hoi, L. Gao, E. Metaxa, D. D. Swartz, and J. Kolega. Complex Hemodynamics at the Apex of an Arterial Bifurcation Induces Vascular Remodeling Resembling Cerebral Aneurysm Initiation. *Stroke*, 38(6):1924–1931, 2007. 2
- [26] M. Neugebauer, V. Diehl, M. Skalej, and B. Preim. Geometric Reconstruction of the Ostium of Cerebral Aneurysms. In *Vision, Modeling, and Visualization*, pages 307–314, 2010. 2, 3
- [27] M. Neugebauer, R. Gasteiger, O. Beuing, and et al. Map Displays for the Analysis of Scalar Data on Cerebral Aneurysm Surfaces. *CGF (EuroVis)*, 28 (3):895–902, 2009. 2
- [28] A. Perez-Garcia, V. Ayala-Ramirez, R. E. Sanchez-Yanez, and J.-G. Avina-Cervantes. Monte Carlo Evaluation of the Hausdorff Distance for Shape Matching. In *Proceedings of the 11th Iberoamerican conference on Progress in Pattern Recognition, Image Analysis and Applications, CIARP'06*, pages 686–695, Berlin, Heidelberg, 2006. Springer-Verlag. 7
- [29] F. H. Post, B. Vrolijk, H. Hauser, R. S. Laramée, and H. Doleisch. Feature Extraction and Visualization of Flow Fields. In *Eurographics*, 2002. 1
- [30] J. Reininghaus, N. Kotava, D. Guenther, J. Kasten, H. Hagen, and I. Hotz. A Scale Space Based Persistence Measure for Critical Points in 2D Scalar Fields. *IEEE TVCG*, 17(12):2045–2052, 2011. 9
- [31] T. Salzbrunn and G. Scheuermann. Streamline Predicates. *IEEE TVCG*, 12(6):1601–1612, 2006. 2
- [32] J. Schöberl. NETGEN: An Advancing Front 2D/3D-Mesh Generator Based on Abstract Rules. *Computing and Visualization in Science*, 1:41–52, 1997. 3
- [33] D. M. Sforza, C. M. Putman, and J. R. Cebral. Hemodynamics of Cerebral Aneurysms. *Annual Review of Fluid Mechanics*, 41:91–107, 2009. 1
- [34] R. van Pelt, J. O. Bescós, M. Breeuwer, R. E. Clough, and M. E. Gröller. Exploration of 4D MRI Blood-Flow Using Stylistic Visualization. *IEEE TVCG*, 16(6):1339–1347, 2010. 2
- [35] R. van Pelt, J. O. Bescós, M. Breeuwer, R. E. Clough, M. E. Groller, B. ter Haar Romenij, and A. Vilanova. Interactive Virtual Probing of 4D MRI Blood-Flow. *IEEE TVCG*, 17(12):2153–2162, 2011. 2, 5
- [36] T. Weinkauff and D. Gnther. Separatrix Persistence: Extraction of Salient Edges on Surfaces Using Topological Methods. *CGF (Proc. SGP)*, 28(5):1519–1528, July 2009. 9
- [37] M. J. Wermer, I. C. van der Schaaf, A. Algra, and G. J. Rinkel. Risk of Rupture of Unruptured Intracranial Aneurysms in Relation to Patient and Aneurysm Characteristics: An Updated Meta-Analysis. *Stroke*, 38(4):1404, 2007. 1